Macro- to nano-scale analysis of an amorphous carbon coating on cemented carbides

Author: Ash Nova Royo, anovaroy7@alumnes.ub.edu
Facultat de Física, Universitat de Barcelona, Diagonal 645, 08028 Barcelona, Spain.

Advisors: Beatriz Vargas Carosi, bvargaca16@alumnes.ub.edu; Sergi Plana Ruiz, sergi.plana@urv.cat; Núria Cinca, nuria.cinca@hyperionmt.com; Francesca Peiró Martínez, francesca.peiro@ub.edu

Abstract: This study characterizes a novel amorphous carbon coating on two cemented carbide substrates with fine (6CoF) and medium-sized (6CoM) tungsten carbide grains, both containing 6 wt% of cobalt binder. These materials are critical as drilling and milling tools in the manufacturing industry due to their exceptional hardness and fracture toughness balance. Samples of the coating-substrate interface were prepared using a focused ion beam and analyzed with advanced transmission electron microscopy techniques. Raman spectroscopy verified the amorphous nature of the coatings, discarding potential FIB-induced amorphization. Energy-dispersive X-ray spectroscopy, selected area electron diffraction, and 4D scanning transmission electron microscopy were employed to analyze the chemical composition and crystallographic structure. While the coatings were predominantly amorphous, the 6CoM sample exhibited a polycrystalline region containing diamond and graphite. Additionally, a $\sim$ 40 nm thick amorphous layer rich in tungsten was identified at the coating-substrate interface in both samples, providing a complete characterization of this important coating-substrate system for the tooling industry.
Keywords: Solid State, Micro and Nanotechnology, TEM, Raman Spectroscopy, Diffraction
SDGs: 9. Industry, Innovation and Infrastructure

I. INTRODUCTION

Diamond is ideal for tool manufacturing and technological advancements due to its exceptional hardness; however, its high cost drives the search for alternative materials with similar properties [1]. One such alternative is diamond-like carbon (DLC), an amorphous carbon composed of sp^2 (graphite-like) and sp^3 (diamond-like) bonds, with a significant sp^3 content. This structure gives DLC excellent hardness, chemical stability, wear resistance and friction reduction, making it widely used in demanding applications [2]. One of the possible methods for producing DLC coatings is Chemical Vapor Deposition (CVD), where a carbon-containing gas decomposes under heat, depositing a thin carbon film on a substrate. Plasma-Assisted CVD (PA-CVD), a notable variant, uses UV radiation to generate radicals from precursor gas molecules, which then react on the material's surface. This enables the formation of high sp^3-content DLC films at lower temperatures, offering improved energy efficiency [3].

Given their excellent mechanical properties, cemented carbide substrates, usually named *hardmetals*, are often chosen as substrates for such coatings. These materials consist of a hard phase—such as carbides, nitrides, or carbonitrides of transition metals from groups 4, 5, and 6 of the periodic table—combined with a metallic binder. The binder, typically cobalt but sometimes nickel or iron, constitutes 3–30 wt% (weight percentage) of the material, providing toughness and ductility, while the hard phase ensures hardness and wear resistance [4].

This study examines a novel amorphous carbon coating developed via PA-CVD on two cemented carbide substrates, both with cobalt (Co) as the binder matrix and differing in tungsten carbide (WC) grain sizes. This difference is significant, as finer grains enhance hardness and wear resistance [4], making it crucial to disentangle coating-substrate interaction in both substrates. Accordingly, Transmission Electron Microscopy (TEM) was employed to achieve nanoscale resolution. High-Resolution TEM (HRTEM) identified critical interface features, like structural continuity and defects, while additional TEM techniques—Energy-Dispersive X-Ray Spectroscopy (EDXS), Selected Area Electron Diffraction (SAED), and 4D Scanning Transmission Electron Microscopy (4D STEM)—enabled a complete chemical and structural characterization of the samples.

II. METHODS

A. Materials and sample preparation

The samples under study consist of two cemented carbides, each coated with a 10–20 μm thick DLC layer. Both substrates contain 6 wt% Co as the metallic binder (6Co) and WC as the hard phase, with the main difference being the WC grain size: one has fine grains (6CoF) and the other has medium grains (6CoM). For simplicity, we will extend the substrate type nomenclature to include the corresponding DLC coating.

For TEM analysis, it was necessary to prepare cross-sections that included both the coating and part of the substrate, thus involving the use of a Focused Ion Beam (FIB) for such accurate preparation.

FIB is a high-precision technique that uses a focused ion beam, typically gallium, to mill, image, or modify materials at the micro- and nanoscale. By directing the

beam onto a surface, combined with a precursor gas, the ions either cause deposition or sputter material away. Scanning electron microscopes (SEM) are often paired with FIB for simultaneous imaging and milling, using a dual beam, an ion beam for milling, and an electron beam for imaging, enabling precise selection and thinning of specific areas.

Two electron-transparent lamellae (thickness$<$100 nm) from sample 6CoF and one from 6CoM were prepared using a ThermoFisher Scios2 DualBeam FIB system, integrated with a high-resolution scanning electron microscope (FESEM-FIB), at the Scientific & Technical Resources Service (SRCIT) of Universitat Rovira i Virgili. During the preparation of the lamellae, the system was first calibrated, and the area of interest was selected. A protective platinum (Pt) layer was then applied in two stages to shield the sample during ion milling. The first Pt layer was deposited using the electron beam, which provided a less aggressive approach but required more time, while the second Pt layer was deposited using the ion beam. Optimization attempts, detailed in the Supplementary Material section, were made during two key steps of the ion milling process:

- **Trenching:** Trenches were milled on either side of the selected region covered by the two Pt deposition layers using the ion beam. The milling parameters were optimized considering the material hardness, with an optimal current value of 7 nA.
- **Thinning:** The lamellae were further thinned to achieve electron transparency, as illustrated in Fig. 1. Careful adjustment of the ion current and voltage showed that higher parameters accelerated the process but caused redeposition and excessive platinum erosion, resulting in thicker lamellae. In contrast, lower parameters took longer but produced thinner lamellae.

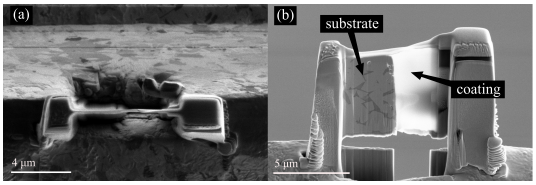

FIG. 1: Images of the 6CoM lamella captured during the final stages of the thinning process. (a) Ion beam scanning image illustrating the extent of thinning (the ion beam is held at 52°). (b) SEM image showing the characteristic polygons of WC in the substrate, along with the coating layer.

B. Raman Spectroscopy

Raman spectroscopy is a non-destructive technique that analyzes the inelastic scattering of photons resulting from their interaction with molecular vibrations or lattice phonons in solids. This method is particularly valuable for characterizing carbon-based materials. In materials containing sp^2-bonded graphitic clusters, resonance effects under visible light excitation enhance Raman scattering, making the spectrum highly sensitive to the structural order of sp^2 carbon [2].

To ensure that the FIB process did not cause amorphization of the samples, Raman spectroscopy was performed at the Scientific and Technological Centers of the University of Barcelona (CCiTUB) using visible light with a wavelength of 532 nm. Measurements consisted of 5 accumulations of 20 seconds each at 10% laser power, which provides good signal quality without damaging the sample, using a 100× objective lens. The analyzed areas had a diameter of approximately 1 µm, and three different regions were examined. The Raman spectra were deconvoluted using the open-source software RAMAN-Deconvolution [5]. For processing, the baseline was removed using a third-degree polynomial fit, followed by spectra deconvolution with the least squares method.

C. TEM

A JEOL F200 microscope, operated at 200 kV with a Gatan OneView CMOS-based camera (4096x4096 pixels), was used for this study at SRCIT. HRTEM was employed to analyze the coating, the substrate, and their interface in greater detail. Annular Bright Field (ABF) and Annular Dark Field (ADF) images were used to measure the grain size of both samples. For each grain, two measurements were taken: the first corresponds to the longest distance within the grain, referred to as the longitudinal axis. The second measurement, taken perpendicular to the longitudinal axis, corresponds to the largest distance within the grain in that direction and is referred to as the transverse axis. Excluding poorly defined grains, a total of 27 grains were measured per sample. TEM data were processed using DigitalMicrograph (Gatan Microscopy Suite), and indexing was conducted with *«Eje z»* software [6] using Fast Fourier Transform (FFT) and SAED. Additionally, EDXS was performed on this microscope for compositional analysis, and 4D STEM was used to capture electron diffraction patterns at each scanned point, providing four-dimensional data (two spatial and two reciprocal space dimensions) [7]. 4D STEM data were processed with DiffGen2 and MapViewer2, programs from the commercial ASTAR software package, to generate phase and orientation maps.

III. RESULTS AND DISCUSSION

A. Raman Spectroscopy

Raman spectroscopy was performed to analyze the 6CoF sample in three different regions, yielding all three

equivalent spectra, similar to those expected for DLC [2]. Fig. 2 shows a representative spectrum from one of the analyzed areas. The experimental deconvolution results were compared with reference data [8], as shown in Table I, to identify the predominant contributions.

The deconvolution revealed contributions from the G band, characteristic of graphite, and the D band, associated with disorder in graphitic lattices, which can be further subdivided into subpeaks. Among these subpeaks, D3, typically associated with amorphous carbon, was the most predominant, confirming the amorphous nature of the coating.

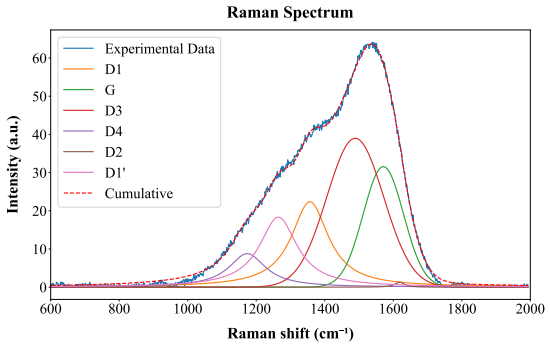

FIG. 2: Deconvoluted Raman spectrum of the sample 6CoF, acquired with $\lambda = 532$ nm. The peaks observed in the figure, as a result of the deconvolution, are explained in Table I. D1' is associated with disorder in graphitic lattices. The G and D3 peaks were fitted with Gaussians, while the others were fitted with Lorentzians.

Band	Raman shift (cm^{-1})			Vibration mode
	6CoF	Disordered Graphite	Highly ordered Graphite	
G	1571 ± 3	~ 1580	~ 1580	Ideal graphitic lattice (E_{2g}-symmetry)
D1 (D)	1357 ± 2	~ 1350	–	Disordered graphitic lattice (graphene layer edges, A_{1g} symmetry)
D2 (D')	1619 ± 3	~ 1620	–	Disordered graphitic lattice (surface graphene layers, E_{2g}-symmetry)
D3 (D")	1490 ± 10	–	–	Amorphous carbon
D4 (I)	1174 ± 3	–	–	Disordered graphitic lattice (A_{1g} symmetry), polyenes, ionic impurities

TABLE I: First-order Raman bands and vibration modes for 6CoF, with graphite reference data taken from [8]. Raman shifts for disordered graphite were measured at 514 nm in the cited study, whereas this work analyzes data at 532 nm.

IV. MORPHOLOGY AND CHEMICAL COMPOSITION ANALYSIS

In agreement with Raman spectroscopy, TEM images confirmed an overall amorphous coating in the samples. The two lamellae examined from 6CoF were entirely amorphous, while the lamellae from 6CoM revealed a polycrystalline region measuring approximately 1.9 μm^2. Fig. 3 provides a general view of the sample and includes EDXS maps, which reveal a uniform W-rich thin layer. TEM analysis indicated that this layer had a thickness of about 40 nm, with a consistent distribution across the interface in both samples, regardless of contact with cobalt or WC grains.

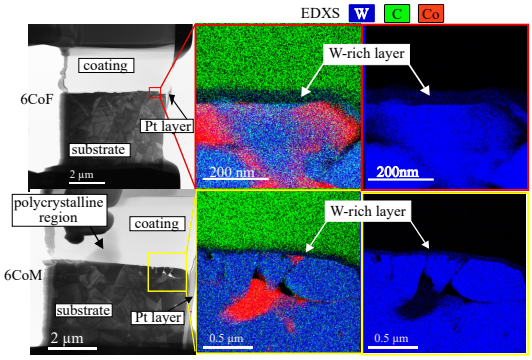

FIG. 3: ABF images of the 6CoF (top) and 6CoM (bottom) lamellae are shown, with EDXS images on the right revealing a thin W-rich layer present in both samples.

Regarding the WC grain size, the 6CoM sample exhibited a larger median grain size (0.9 µm longitudinal, 0.6 µm transverse) compared to the 6CoF (0.5 µm longitudinal, 0.3 µm transverse), as expected. Both samples displayed some variability in grain size. In particular, the 6CoF sample substrate contained a few abnormally large grains compared to the rest, see Fig. 4.

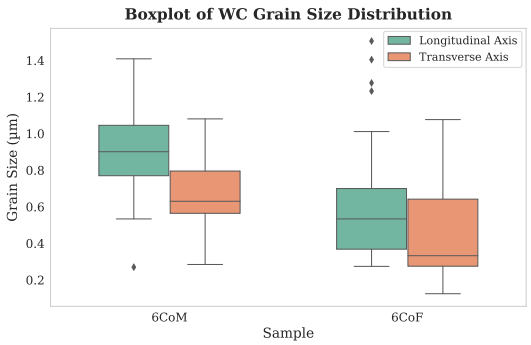

FIG. 4: Boxplot comparing WC grain size distributions in the 6CoM and 6CoF samples along the longitudinal and transverse axes.

V. STRUCTURAL CHARACTERIZATION

SAED, 4D STEM and HRTEM were employed to obtain structural insights into the samples. SAED confirmed the amorphous nature of the coating along

the layer, with the exception of the polycrystalline area observed in the 6CoM sample. This polycrystalline region was identified as a mixture of crystalline diamond and graphite, assuming lattice parameters $a_{\text{diamond}} = 3.567$ Å (cubic symmetry, space group $Fd\bar{3}m$) and $a_{\text{graphite}} = 2.461$ Å, $c_{\text{graphite}} = 6.708$ Å (hexagonal symmetry, space group $P6_3/mmc$), respectively, as summarized in Fig. 5 and Table II.

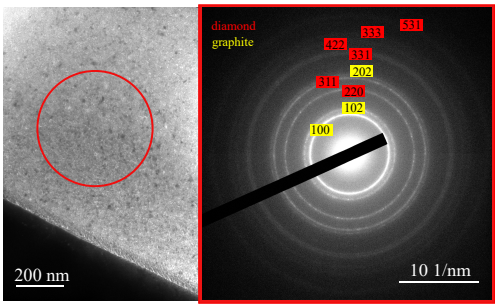

FIG. 5: Diffraction pattern of the 6CoM sample in the polycrystalline zone, showing a mixture of diamond and graphite. For overlapping rings (see Table II), the *hkl* Miller indices shown in the SAED pattern correspond to the structure with the smallest d-spacing error relative to the theoretical value.

Experimental d spacing (Å) ± 0.05	**Theoretical diamond d spacing (Å)**	**Diamond hkl**	**Theoretical graphite d-spacing (Å)**	**Graphite hkl**
2.11	2.06	111	2.13	100
1.82	–	–	1.80	102
1.27	1.26	220	–	–
1.09	1.08	311	1.07	200
1.03	–	–	1.02	202
0.80	0.82	331	0.80	211
0.73	0.73	422	–	–
0.68	0.69	333	–	–
0.59	0.60	531	–	–

TABLE II: Comparison of the experimental d-spacing values obtained from the SAED pattern in the polycrystalline region of sample 6CoM with the theoretical values for diamond and graphite. The results indicate contributions from both diamond and graphite, with several d-spacing values potentially corresponding to either structure.

To characterize the interface, 4D STEM was employed, providing phase and orientation maps of the analyzed areas, as shown in Fig. 6 and 7. Dark areas in the phase and orientation maps represent regions of low reliability. Colormaps illustrate the symmetrically-independent directions according to the Laue class of the corresponding space group. For both samples, the predominant phase was hexagonal tungsten carbide (WC $P\bar{6}m2$). The presence of trigonal tungsten semicarbide (W_2C $P\bar{3}$) was also suggested to be near or potentially merged with the W-rich thin layer observed in the EDXS data. However, the amorphous nature of this layer reduced the accuracy of the software calculations, as the program relies on crystalline diffraction patterns, resulting in lower reliability for this identification. At the interface, WC $P\bar{6}m2$ demonstrated a preferred orientation in both samples, corresponding to the orange regions in the orientation maps shown in Fig. 6, with crystallographic directions $[3\bar{2}\bar{2}]$ in 6CoF and $[\bar{7}74]$ in 6CoM. Regarding the binder matrix, two cobalt phases were observed: the cubic (Co $Fm\bar{3}m$), which predominated, and the hexagonal (Co $P6_3/mmc$).

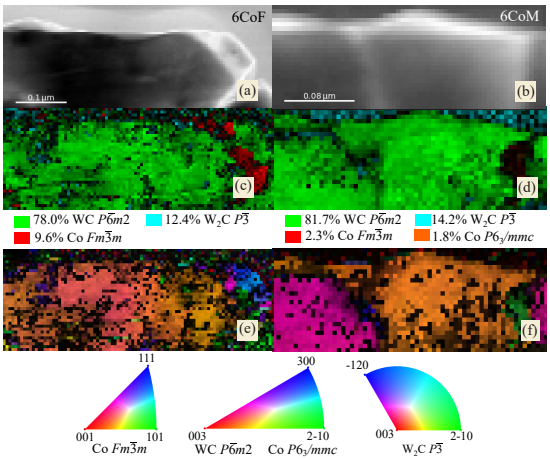

FIG. 6: Left column: 6CoF; right column: 6CoM. (a, b) Virtual bright-field images; (c, d) phase maps; (e, f) orientation maps.

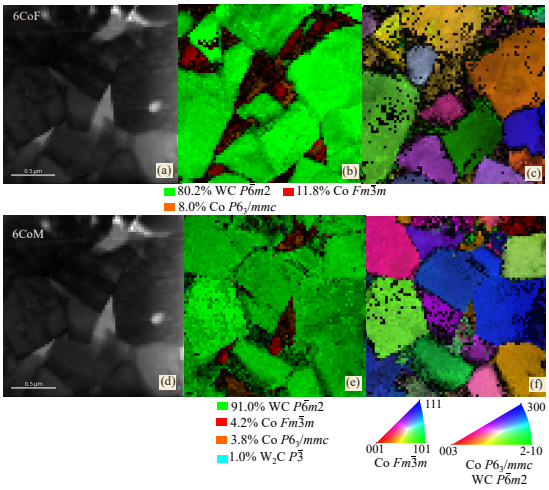

FIG. 7: Top row: 6CoF; bottom row: 6CoM. (a, d) Virtual bright-field images; (b, e) phase maps; (c, f) orientation maps.

High-resolution images revealed that the 6CoM lamella exhibits less uniformity at the interface compared to 6CoF. Despite this difference, the ∼40 nm W-rich layer at the interface remains relatively consistent in both samples. As shown in Fig. 8, the amorphous diffraction pattern of the carbon coating displays diameters and features of the diffuse rings that differ from those of the W-rich layer, confirming their distinct nature. This figure also shows the polycrystalline region of the 6CoM sample, where various small grains can be observed; one

of them corresponds to the graphite structure in the [101] orientation, consistent with the SAED data, which indicates the presence of a mixture of small graphite and diamond grains in the area.

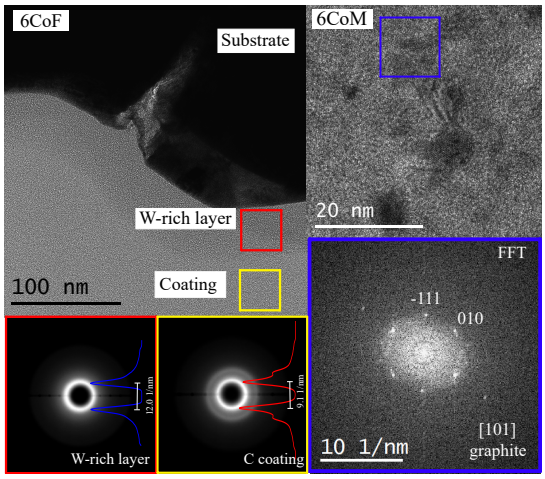

FIG. 8: Left: Amorphous diffraction pattern of 6CoF extracted via 4D STEM, along with the intensity profile of the diffuse rings, highlighting the differences between the W-rich layer and the carbon coating. Right: Polycrystalline coating region in 6CoM with an FFT displaying a hexagonal graphite diffraction pattern.

VI. CONCLUSIONS

In this work we have accomplished an exhaustive chemical and structural characterization using advanced TEM techniques to compare two amorphous carbon coatings on cemented carbide substrates with different tungsten carbide grain sizes. This characterization revealed that the 6CoF coating was entirely amorphous, while 6CoM exhibited a small polycrystalline region of diamond and graphite embedded within the amorphous matrix. The substrate-coating interface appeared rougher in the 6CoM sample than in the 6CoF. Nevertheless, both samples contained a thin W-rich layer, approximately 40 nm thick, at the interface, regardless of whether it was in contact with the cobalt binder matrix or the tungsten carbide grains.

As expected, 6CoF exhibited finer grains than 6CoM, with the grains oriented in various directions. The directions near the interface corresponded to the crystallographic directions of $[3\bar{2}\bar{2}]$ in 6CoF and $[\bar{7}74]$ in 6CoM, as determined through 4D STEM. This technique also confirmed hexagonal tungsten carbide as the predominant phase. Additionally, two cobalt phases were observed: cubic cobalt, which was the dominant binder phase, and hexagonal cobalt.

Overall, (S)TEM has proven to be a highly suitable technique for analyzing this important material in the metallurgy industry, where nanoscale precision was essential to properly characterize the interface between the coating and the substrate.

Acknowledgments

A special thank you to Beatriz Vargas Carosi for her endless patience, dedication, and for being there every single step of the way. I would like to thank as well Sergi Plana Ruiz for sharing his knowledge of TEM and his passion for 4D STEM, to Núria Cinca for providing the samples and explaining their basic details, to Francesca Peiró Martínez, especially for giving me the opportunity to work with her team, and to Sonia Estradé Albiol for her guidance during meetings. Thanks also to the SRCiT and CCiTUB technical staff for their invaluable assistance. Lastly, heartfelt thanks to my parents and partner for their unwavering support.

[1] X. Wang and J. Ye, *Interface characteristics of CVD diamond coating on WC-Co cemented carbide substrate*, Surface and Coatings Technology, **485**, 130886 (2024). DOI: 10.1016/j.surfcoat.2024.130886.

[2] A. C. Ferrari and J. Robertson, *Raman spectroscopy of amorphous, nanostructured, diamond-like carbon, and nanodiamond*, Philosophical Transactions of the Royal Society A: Mathematical, Physical and Engineering Sciences, **362**(1824), 2477–2512 (2004). DOI: 10.1098/rsta.2004.1452.

[3] F. Ojeda, F. J. Marti, and J. M. Albella, *Preparación de recubrimientos cerámicos mediante técnicas de CVD*, Boletín de la Sociedad Española de Cerámica y Vidrio, **37**(6), 447–453 (1998). DOI: 10.3989/cyv.1998.v37.i6.984.

[4] J. García, V. Collado Ciprés, A. Blomqvist, and B. Kaplan, *Cemented carbide microstructures: A review*, International Journal of Refractory Metals and Hard Materials, **80**, 40–68 (2019). DOI: 10.1016/j.ijrmhm.2018.12.004.

[5] MacDumi, *RAMAN-Deconvolution* [Computer software]. GitHub (n.d.). `https://github.com/MacDumi/RAMAN-Deconvolution`.

[6] J. A. Pérez, *TEM-UCA Software*, University of Cádiz, (2018). Available: `http://www.uca.es/tem-uca`.

[7] C. Ophus, *Four-dimensional scanning transmission electron microscopy (4D-STEM): From scanning nanodiffraction to ptychography and beyond*, Microscopy and Microanalysis, **25**(3), 563–582 (2019). DOI: 10.1017/s1431927619000497.

[8] A. Sadezky, H. Muckenhuber, H. Grothe, R. Niessner, and U. Pöschl, *Raman microspectroscopy of soot and related carbonaceous materials: Spectral analysis and structural information*, Carbon, **43**(8), 1731–1742 (2005). DOI: 10.1016/j.carbon.2005.02.018.

Preparació del manuscript del TFG amb LaTeX

Author: Ash Nova Royo, anovaroy7@alumnes.ub.edu
Facultat de Física, Universitat de Barcelona, Diagonal 645, 08028 Barcelona, Spain.

Advisors: Beatriz Vargas Carosi, bvargaca16@alumnes.ub.edu; Sergi Plana Ruiz, sergi.plana@urv.cat; Núria Cinca, nuria.cinca@hyperionmt.com; Francesca Peiró Martínez, francesca.peiro@ub.edu

Resum: Aquest estudi se centra en la caracterització de la interfície entre un nou recobriment de carboni amorf i dos tipus de substrats de carbur cimentat. Els substrats estan formats per una matriu metàl·lica de cobalt (6% en pes) i una fase dura de carbur de tungstè (WC), diferenciant-se per la mida dels grans de WC: la mostra 6CoF presenta grans més fins, mentre que la 6CoM en té de mitjans. Aquests materials són altament valorats en la fabricació d'eines de perforació i fresat gràcies a la seva gran duresa i resistència al desgast. Per analitzar la interfície, s'han utilitzat tècniques avançades com la microscòpia electrònica de transmissió (TEM), amb preparació prèvia mitjançant feix d'ions focalitzat (FIB). L'espectroscòpia Raman ha confirmat la naturalesa amorfa dels recobriments, descartant alteracions degudes al procés de preparació. Així mateix, s'han emprat espectroscòpia de dispersió d'energia de raigs X (EDXS), difracció electrònica en àrea seleccionada (SAED) i microscòpia electrònica de transmissió d'escaneig en 4D (4D STEM) per caracteritzar la composició química, les fases cristal·logràfiques i l'orientació dels materials, respectivament. Els resultats revelen que el recobriment de la mostra 6CoF és completament amorf, mentre que el de la 6CoM conté una petita regió policristal·lina amb diamant i grafit. Totes dues mostres presenten una capa amorfa uniforme rica en tungstè d'uns 40 nm de gruix a la interfície, independentment del contacte amb la matriu de cobalt o amb els grans de WC. Tanmateix, la mostra 6CoM presenta més irregularitats en la interfície en comparació amb la uniformitat observada a la 6CoF. Les observacions mitjançant 4D STEM han determinat que la fase predominant és el carbur de tungstè hexagonal (WC, $P\bar{6}m2$). Les direccions presentades pels grans de WC propers a la interfície corresponen a les direccions cristal·logràfiques $[3\bar{2}\bar{2}]$ en 6CoF i $[\bar{7}74]$ en 6CoM. També s'han identificat dues fases de cobalt: la cúbica (Co, $Fm\bar{3}m$), que és la principal, i l'hexagonal (Co, $P6_3/mmc$), que es troba en menor mesura. La present caracterització demostra que les tècniques basades en (S)TEM són essencials per analitzar amb precisió nanomètrica la interfície entre el recobriment i el substrat, oferint informació detallada sobre la composició i estructura, entenent així les seves propietats.
Paraules clau: Estat Sòlid, Micro i Nanotecnologia, TEM, Espectroscòpia Raman, Difracció
ODSs: Aquest TFG està relacionat amb els Objectius de Desenvolupament Sostenible (SDGs)

Objectius de Desenvolupament Sostenible (ODSs o SDGs)

1. Fi de la es desigualtats		10. Reducció de les desigualtats	
2. Fam zero		11. Ciutats i comunitats sostenibles	
3. Salut i benestar		12. Consum i producció responsables	
4. Educació de qualitat		13. Acció climàtica	
5. Igualtat de gènere		14. Vida submarina	
6. Aigua neta i sanejament		15. Vida terrestre	
7. Energia neta i sostenible		16. Pau, justícia i institucions sòlides	
8. Treball digne i creixement econòmic		17. Aliança pels objectius	
9. Indústria, innovació, infraestructures	X		

SUPPLEMENTARY MATERIAL

A. FIB parameters

Sample		6CoF		
Template		Top-down template (15 nA current)		
Correction factor		3		
Protective layer		2 µm (Pt)		
Thinning				
Tilt	**Current**	**Voltage**	**Z**	**Lamella's thickness**
± 2	0.5 nA	30 kV	20 µm	914 nm
± 1.8	0.1 nA	30 kV	20 µm	290 nm
± 1.8	50 pA	16 kV	20 µm	$\lesssim$ 100 nm
± 5	48 pA	5 kV	-	Dynamic all directions

TABLE III: Summary of focused ion beam (FIB) parameters for the preparation of lamellae. A top-down template and a correction factor of 3 (compared to 1 for silicon) were applied during trench formation; however, the template for hard samples proved more effective. Thinning parameters outline the beam tilt, current, voltage, and resulting lamella thickness at various steps of the thinning process. Higher current and voltage expedited thinning but caused faster erosion of the platinum protective layer, resulting in a final lamella thicker than desired. In the final step, low current and voltage were applied dynamically in all directions to refine the lamella.

Sample		6CoF		
Template		Hard samples (7 nA current)		
Correction factor		1.6		
Protective layer		2 µm (Pt)		
Thinning				
Tilt	**Current**	**Voltage**	**Z**	**Lamella's thickness**
± 2	0.5 nA	30 kV	15 µm	914 nm
± 2	0.3 nA	30 kV	15 µm	290 nm
± 2	0.1 nA	30 kV	12 µm	-
± 1.3	50 pA	16 kV	10 µm	$\lesssim$ 90 nm
± 3	48 pA	5 kV	15 s	Dynamic all directions
± 5	27 pA	2 kV	15 s	Dynamic all directions

TABLE IV: Summary of focused ion beam (FIB) parameters for the preparation of lamellae. A hard-sample template and a correction factor of 1.6 were applied during trench formation; however, a correction factor of 2 would have been more effective, as the trenches were difficult to form. Thinning parameters outline the beam tilt, current, voltage, and resulting lamella thickness at different stages of the process. Lower current and voltage steps resulted in slower erosion of the protective layer, leading to a thinner lamella but requiring more time. In the final steps, low current and voltage were applied dynamically in all directions to refine the lamella.

Sample		6CoM		
Template		Hard samples (7 nA current)		
Correction factor		2		
Electron deposition thickness		$\sim$ 200 nm (Pt)		
Protective layer		2 µm (Pt)		
Thinning				
Tilt	**Current**	**Voltage**	**Z**	**Lamella's thickness**
± 2	0.5 nA	30 kV	10 µm	700 nm
± 2	0.3 nA	30 kV	13 µm	$\sim$ 300 nm
± 2	0.1 nA	30 kV	13 µm	$\sim$ 150 nm
± 1.3	50 pA	16 kV	12 µm	$\lesssim$ 70 nm
± 3	48 pA	5 kV	20 s	Dynamic all directions
± 5	27 pA	2 kV	15 s	Dynamic all directions

TABLE V: Summary of focused ion beam (FIB) parameters for the preparation of lamellae. A hard-sample template, operating at a current of 7 nA, with a correction factor of 2, was applied during trench formation, resulting in improved performance for this sample compared to others. Thinning parameters outline the beam tilt, current, voltage, and resulting lamella thickness at different stages of the process. Lower current and voltage steps resulted in slower erosion of the protective layer, leading to a thinner lamella but requiring more time. In the final steps, low current and voltage were applied dynamically in all directions to refine the lamella.